Chapter 9
Synchrotron X-ray Study on Plaston in Metals

Hiroki Adachi

Methods that can be used to reinforce metal include solid solution strengthening (Fleischer 1963), precipitation strengthening (Gerold and Harberkorn 1966), dislocation hardening (Bailey and Hirsch 1960), and grain refining (Petch 1953; Hall 1951). In particular, in grain refining, as expressed in the Hall–Petch equation, the strength of the material increases linearly as the crystal grain becomes finer. As the process does not inevitably require the addition of many elements, it is suitable for use in recycling, lessens the load on the environment, and consequently has recently attracted attention as a method for reinforcing structural metal materials. Another reason for the increased focus on grain refining is that the development of a severest plastic deformation method allows a relatively easy preparation of submicron grain metal crystals (Valiev et al. 2000; Tsuji et al. 2002; Huang et al. 2003; Horita and Langdon 2005; Ferrasse 1997).

The ultra-fine grained (UFG) materials thus obtained exhibit significantly high strength as well as unique mechanical characteristics, such as the extra-hardening phenomenon (Kamikawa et al. 2003, 2009), the hardening-by-annealing phenomenon (Huang et al. 2006), and the yield-point-drop phenomenon (Kamikawa et al. 2003, 2009), in AI alloys. In the extra-hardening phenomenon, when the crystal grain size falls below a few micrometers, the strength of the UFG material increases beyond that represented by a line extended from the slope of the Hall–Petch plot. Although with coarse-grained (CG) materials, the hardening-by-annealing phenomenon results in recovery and recrystallization, and since there is decreased dislocation density, which results in decreased strength and increased ductility, with UFG materials, this phenomenon causes an entirely opposite change of increasing the strength of the material and decreasing its ductility. Moreover, while

H. Adachi (✉)
Department of Materials and Synchrotron Radiation Engineering, University of Hyogo, Himeji, Japan
e-mail: adachi@eng.u-hyogo.ac.jp

© The Author(s) 2022

I. Tanaka et al. (eds.), *The Plaston Concept*,
https://doi.org/10.1007/978-981-16-7715-1_9

the yield-point-drop phenomenon is observed in steel materials with a BCC structure, normally, because Al alloys with a face-centered cubic (FCC) structure show a continuous decrease, they show no yield-point-drop phenomenon. However, yield point drop has been reported in UFG Al alloys. Otherwise as well, for super-fine-grain materials, it has been reported that the strain rate dependence of yield strength becomes very large.

As aforementioned, UFG materials exhibit unique mechanical characteristics, believed to be a result of their mechanism of plastic deformation being different from that of CG materials. One reason for this difference is thought to be their significantly high grain densities compared to those of CG materials. Plastic deformation in CG materials occurs due to dislocations, which gradually increase inside grains. However, in UFG materials, deformation also occurs due to the formation of nanotwin crystals generated from the grain boundary and stacking faults. Another reason is thought to be the difference in the behavior of dislocations inside the grains from CG materials. We referred the components of deformation as "*Plaston,*" and this study aims to improve the strength and ductility of metallic materials by understanding plastons.

The first approach is to understand the extent to which the unique mechanical characteristics of UFG materials can be explained by dislocation motion and to which they cannot. That is, there is a need to understand whether the characteristics must be explained using conceptions of plastons other than dislocation. It has been indicated that nanotwins and stacking faults can occur at grain boundaries in UFG materials (Lu et al. 2005; Shen et al. 2005; Chen et al. 2003), so dislocation can both occur and disappear at the grain boundaries (Mompiou et al. 2012). For this reason, it is necessary to conduct research while considering the possibility that the dislocation substructure might differ during deformation and after unloading, and thus it is desirable to conduct in situ measurements. To date, there have been examples described in the literature where the behavior of dislocations during deformation was observed using a transmission electron microscope (TEM). However, the films for TEM observations are extremely thin and the surface effect on the dislocation motion cannot be neglected. Therefore, it is desirable to use bulk materials for such measurements. For this reason, in situ X-ray diffraction (XRD) measurements were conducted during the deformation of materials at SPring-8, the largest synchrotron radiation facility, and the effect of the crystal grain size on the dislocation behavior was studied (Adachi et al. 2015, 2016; Miyajima et al. 2016; Nakayama et al. 2016), [39].

The synchrotron radiation at SPring-8 exhibits high flux, which enables the measurement of the diffraction intensity with a high signal-to-noise (S/N) ratio within a short time. Furthermore, a detector with a large area enables multiple diffraction peaks to be collected simultaneously, making it possible to carry out in situ measurements with high temporal resolution and record diffraction peaks over a large diffraction angle range within ~0.5 s. Additionally, synchrotron radiation exhibits high directivity, which reduces the effect of the instrumental function on the XRD measurement results and represents an advantage of synchrotron radiation. The Williamson–Hall method is used for calculating the dislocation density from the

obtained XRD diffraction profile, expressed as

$$\frac{\Delta 2\theta_{hkl} cos\theta}{\lambda} = \frac{0.9}{D} + 2\epsilon \frac{sin\theta_{hkl}}{\lambda},$$

where θ is the diffraction peak angle, Δ2θ is the full width at half maximum, and D is the crystallite size, which can be obtained from the reciprocal of the intercept of the Williamson–Hall plot, where θ and Δ2θ values of multiple diffraction peaks from the XRD measurements are used to construct a Williamson–Hall plot, with 2sinθ/λ on the horizontal axis and Δ2θcosθ/λ on the vertical axis. The inhomogeneous strain, ε, in the crystallite can be obtained from the slope of the plot. Assuming that the inhomogeneous strain is a result of dislocation, the dislocation density can be calculated using either of the following equations, (9.1) or (9.2). Here, the coefficient in Eq. (9.1) has a value of 16.1 for the FCC structure and that of 14.4 for the BCC structure. Since the goal here is to compare CG and UFG materials, Eq. (9.1) is chosen because it is difficult to accurately obtain the crystallite size, D, for CG materials, which is a required parameter in Eq. (9.2) (Williamson and Hall 1953; Williamson and Smallman 1956, 1954).

$$\rho = 16.1\left(\frac{\varepsilon}{b}\right)^2 \tag{9.1}$$

$$\rho = \frac{2\sqrt{3\varepsilon}}{Db}. \tag{9.2}$$

Figure 9.1 shows the change in the dislocation density during tensile deformation in a 2 N-aluminum alloy with a crystal grain size of 0.5 μm, formed using the ARB method. As the deformation progresses, the dislocation density changes through four regions. In the first region (region I), the dislocation density does not increase. As the stress increases linearly with macrostrain, it is said to be an elastic deformation region. In the second region (region II), the dislocation density increases rapidly, showing the start of plastic deformation, where stress at this time is denoted by σI. For this reason, the stress σ_I at the boundary between regions I and II can be recognized as the yield stress when the dislocation starts to increase from the dislocation source. The increase in dislocations in region II is almost linear with that in the macrostrain, but the system transitions to the third region (region III) when the dislocation density reaches a certain value (ρ_{II}). The increase in dislocations in region III is slower than that in region II. However, it is not that the rapid increase in the dislocation density in region II gradually slows down as the system enters region III, but rather that the increase in dislocation density suddenly becomes slower when it reaches a certain value ($\rho_{II} = 9.1 \times 10^{14}$ m^{-2}). The significance of parameter ρ_{II} will be discussed later. Unlike in region II, the dislocation density slowly changes in region III. Next, the dislocation density suddenly decreases with unloading associated with fracture. This decrease indicates the occurrence of region IV. Since the time resolution of the experiment is 2 s, the dislocation density decreases to a quarter of that value during deformation

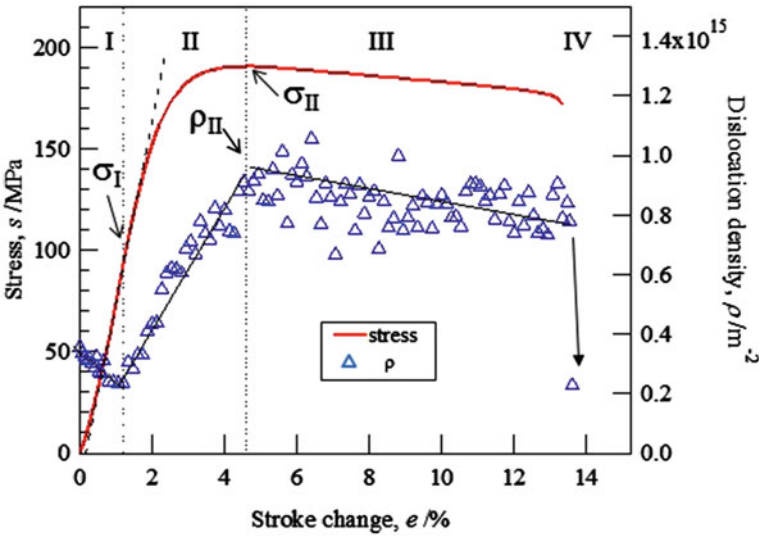

Fig. 9.1 Change in the dislocation density with the nominal strain for ARBed Aluminum during the in situ XRD measurement. Reproduced from (Adachi et al. 2020) and (Adachi et al. 2021) by permission of The Japan Institute of Light Metals

in less than 2 s, reaching the same level as that before the deformation. This is likely because, in UFG materials with a high grain boundary density, the boundary always exists close to the intra-grain dislocations, which leads to dislocations being annihilated, with the grain boundary acting as the sink in the unloading (Williamson and Smallman 1954). This means that in UFG materials, the dislocation substructure is quite different during deformation and after unloading, and that it is difficult to observe the structure during deformation by studying the dislocation substructure after unloading using an electron microscope. This can lead to a misunderstanding that even at room temperature, the driving component of the deformation in UFG materials is not dislocation, but other plastons, such as boundary sliding.

Figure 9.2a shows the changes in the dislocation density during tensile deformation of a 2 N-aluminum CG material with a grain size of 20 μm, formed by annealing a UFG material. Figure 9.2b shows the enlarged view around the low-strain side. In a CG material, the dislocation density also changes through four regions. However, region I, the elastic deformation region, is very short, and dislocations start to increase once the stress reaches 15 MPa (=σ_I), whereby the system transitions to region II. The fact that $\sigma_I = 102$ MP for the UFG material with a grain size of 0.5 μm shows that the dislocation source is activated at very low stress, and dislocations start to increase. In region II, the dislocations rapidly increase, just as in UFG materials, and the increase in the dislocation density becomes slow when it reaches a certain value ($\rho_{II} = 1.57 \times 10^{14}$ m^{-2}). The value of ρ_{II} is about one-sixth that of the UFG material, which is very small, and the system quickly reaches ρ_{II} after entering region II, so region II is barely observed. In region III, the dislocation density increases more

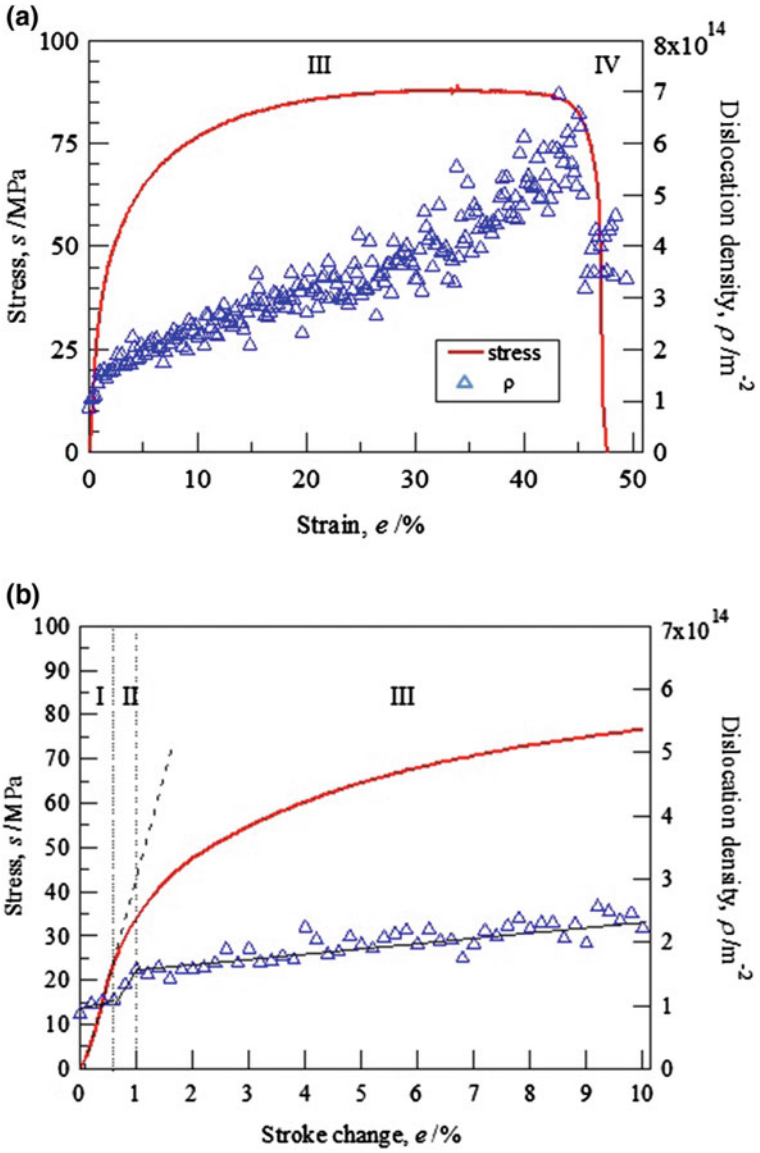

Fig. 9.2 Change in the dislocation density with the nominal strain for coarse-grained Al during the in situ XRD measurement. Reproduced from [22] and [39] by permission of The Japan Institute of Light Metals

slowly than that in region II and achieves a value of ~6×10^{14} m^{-2} right before the fracture. Next, as in UFG materials, the dislocation density increases more slowly with unloading associated with the fracture. However, the reduced amount is about half the increase in region III, and the dislocation density is much higher than that before the tension occurs. This is because the low grain boundary density in the CG material leads to little dynamic recovery. This shows that for the CG material, it is more or less possible to analogize the dislocation substructure during deformation, based on the dislocation substructure observed after unloading.

In the UFG material, the dislocation density rapidly increases in region II and does not increase much in region III, and the flow stress also does not increase. In contrast, for the CG material, the dislocation density significantly increases in region III, leading to an increase in the flow stress. Dislocations arise from the dislocation source in region III of the UFG material, but dynamic recovery, in which annihilation of the grain boundary as the sink occurs, progresses equally as fast, resulting in their balancing each other. As a result, the dislocation density hardly increases in region III, and the flow stress does not increase at all. Therefore, there is no work hardening in region III in the UFG material, which causes plastic instability and low ductility. On the other hand, in the CG material, there is little dynamic recovery due to the low grain boundary density, so the dislocation density significantly increases in region III and work hardening occurs, resulting in high ductility.

Next, a Ni with FCC structure is used to form even finer crystal grains because aluminum has a low melting point and low stacking fault energy, which leads to dynamic recovery during plastic deformation processing, and because it is difficult to reduce the diameters of the crystal grains of 2 N-aluminum via severe plastic deformation processing. Figure 9.3 shows the changes in dislocation density during tensile deformation in UFG nickel with a crystal grain size of 270 nm formed using ARB processing. The dislocation density of the UFG nickel also transitions through four regions, where in situ XRD measurements can be used to obtain the values of σ_I, ρ_{II}, and σ_{II}. For this material, the value of ρ_{II} is as high as 1.6×10^{15} m^{-2}, which is 1.8 times higher than that of the UFG aluminum with a particle diameter of 500 nm. Another difference between this material and the UFG aluminum with a grain diameter of 500 nm is that the dislocation density gradually increases in region III, which is likely to be because of nickel having a higher melting point than aluminum, and thus a lower stacking fault energy, resulting in slow dynamic recovery. However, in region IV, the unloading associated with fracture causes the dislocation density to instantaneously drop to a value close to that observed before the application of tension, and the dislocation substructure during the deformation of a UFG material is significantly different from that after unloading.

It is difficult to obtain finer nanocrystal grains using top-down methods such as high-strain processing (Dao et al. 2007; Liao et al. 2006), and thus a bottom-up method is required. Representative bottom-up strategies include electrolytic deposition, amorphous crystallization, and nanopowder solidification molding methods, which can produce a material with crystal grains of a single nanometer to a few tens of nanometers, sizes unobtainable via severe plastic deformation processing. Aluminum is a base metal, and a solution cannot be used as the electrolytic bath in

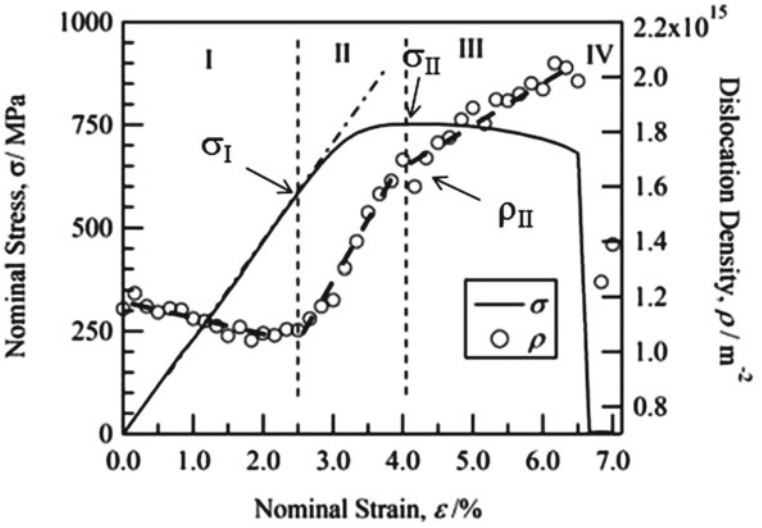

Fig. 9.3 Change in the dislocation density with the nominal strain for ARBed Ni during the in situ XRD measurement. Reproduced from (Adachi et al. 2016) by permission of The Japan Institute of Metals and Materials

the electrolytic deposition method, so the electrolytic deposition method is instead used to produce a nanocrystalline nickel material. A Watt bath is used with nickel sulfate hexahydrate to produce nickel nanocrystals with a crystal grain size of 50 nm (Schuh et al. 2002). Figure 9.4 shows the changes in dislocation density during tensile deformation for the nickel nanocrystals (Adachi et al. 2016). Like the CG and UFG materials, there are four regions in the dislocation density profile of the nickel nanocrystals (NC), where region II with a rapid increase in the dislocation density is extremely long and the dislocation density when moving between regions II and III has a ρ_{II} value of approximately 1.15×10^{16} m^{-2}, which is quite large compared to those of UFG nickel and CG aluminum. Moreover, as with UFG material, in region IV, unloading associated with fractures causes the dislocation density to decrease to a level observed before deformation, indicating that the dislocation substructure of the NC grains after unloading is significantly different from that during deformation.

In all of the in situ XRD measurements of materials, ranging from the coarse-grain aluminum with a particle size of 20 μm to the nanocrystalline nickel with a particle size of 50 nm, as described above, the dislocation density passes through four regions and the instantaneous decrease at the time of unloading associated with fracture becomes apparent as the grain size decreases. Let us consider what is signified by the ρ_{II} value required by in situ XRD measurement. Figure 9.5 shows the change in ρ_{II}, obtained via XRD measurements, of 2 N-Al with changing grain size, where the values for pure Ni are also assembled and shown. For grain sizes larger than 3 μm, ρ_{II} is almost constant at around 10^{14} m^{-2}, but when the grain size is less than 3 μm, ρ_{II} can be understood to be more or less proportional to the inverse

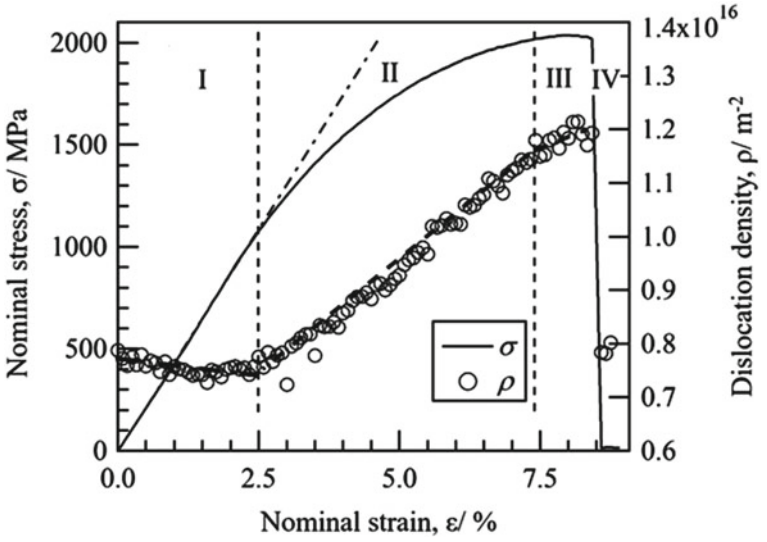

Fig. 9.4 Change in the dislocation density with the nominal strain for electrodeposited Ni during the in situ XRD measurement. Reproduced from (Adachi et al. 2016) by permission of The Japan Institute of Metals and Materials

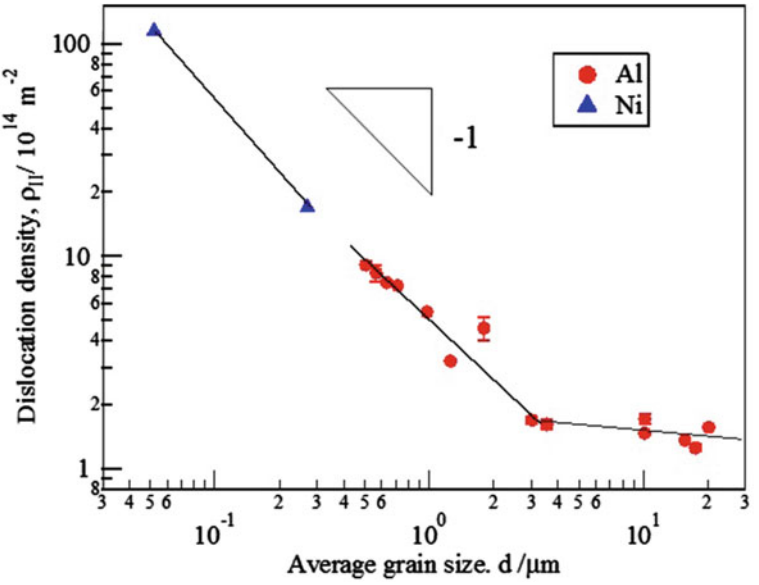

Fig. 9.5 The ρ_{II} as a function of grain size for pure Ni alloys and pure aluminum alloys. Reproduced from (Adachi et al. 2020) and (Adachi et al. 2021) by permission of The Japan Institute of Light Metals

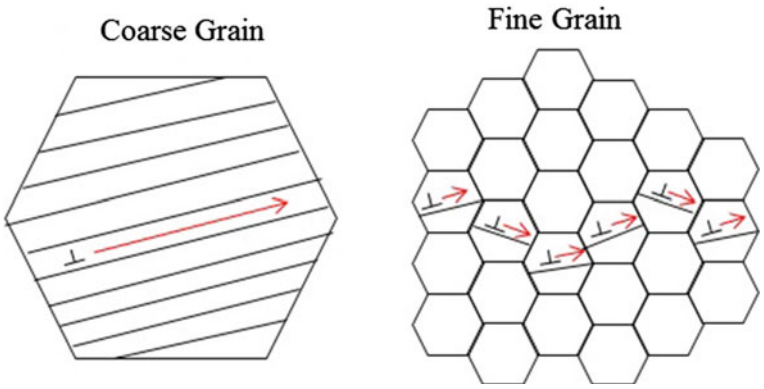

Fig. 9.6 Schematic illustration showing the change in mean free path of dislocation due to grain size. Reproduced from (Adachi et al. 2020) and (Adachi et al. 2021) by permission of The Japan Institute of Light Metals

of the grain size. This can be explained as follows. The relationship between the dislocation density and shear deformation, γ, per unit time by plastic deformation is

$$\gamma = \rho \mathrm{bx}, \tag{9.3}$$

where b is the magnitude of Burger's vector and x is the mean free path. As shown in Fig. 9.6, x is large in the CG material and decreases in order for the increase in grain boundary density, which interferes with the dislocation motion, along with grain refinement. In other words, the dislocation density for plastic deformation increases as a result of grain refinement, and assuming that x is proportional to the particle size, the dislocation density is inversely proportional to the grain size, thus explaining the result in Fig. 9.5. The parameter x does not increase indefinitely with increasing grain size, but if the speed of dislocation motion is found to have an upper limit, then x likewise has an upper limit. Thus, there is a lower limit for ρ, which seems to be reached for particle sizes larger than 3 μm. Therefore, ρ_{II} is the least dislocation density necessary for deformation to occur only due to plastic deformation, and region II can be said to expand rapidly until this dislocation density is reached. Once it reaches ρ_{II}, dislocation no longer needs to increase so rapidly, so its growth slows, as does the growth speed of the dislocations, and the system transitions to region III. In addition, in region II, deformation cannot solely be achieved via plastic deformation, and elastic deformation makes up for the deficit, so the stress increases corresponding to elastic deformation. In other words, both regions II and III are plastic deformation regions. However, note that there is elastic deformation in region III as well, due to an increase in the flow stress caused by an increase in the dislocation density. For coarse crystal grains, the value of ρ_{II} is very small and is achieved rather quickly, leading to a short region II, and for fine grains, ρ_{II} is large, leading to a longer region II. Therefore, while region II is not so significant for CG materials, it needs

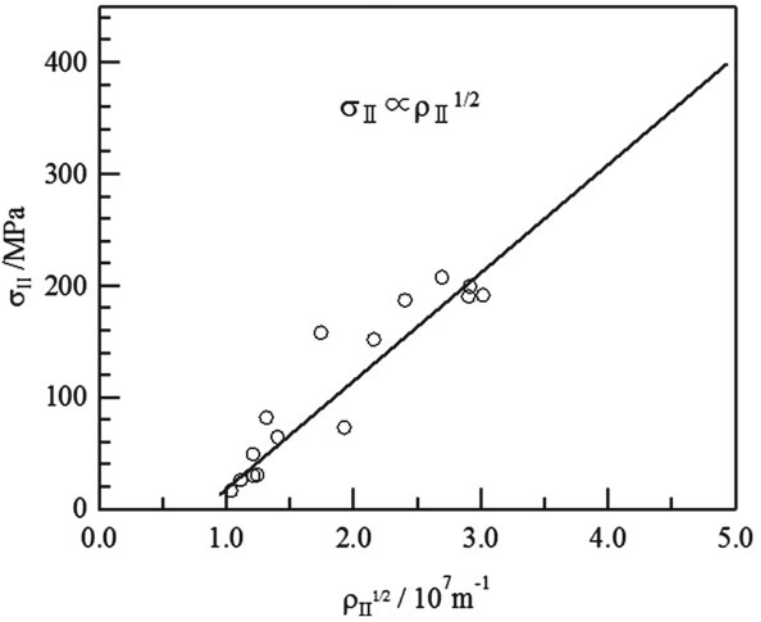

Fig. 9.7 The σ_{II} as a function of square root of ρ_{II} for pure aluminum alloys. Reproduced from (Adachi et al. 2020) and (Adachi et al. 2021) by permission of The Japan Institute of Light Metals

to be considered to understand the mechanical characteristics of UFG materials. For example, in UFG materials, a low initial dislocation density due to annealing leads to a small extent of plastic deformation in region II compared to a case with larger initial dislocations as a result of processing, resulting in a large elastic deformation and stress. However, the flow stress in region III depends on the dislocation density at the time and not on the initial dislocation density. Therefore, in UFG materials with low initial dislocation density, the stress in region II is greater than that in region III, making a yield point drop more probable.

Next, the relationship between the ρ_{II} of 2 N-aluminum with various-sized crystal grains and the stress σ_{II} is examined, as shown in Fig. 9.7. σII is proportional to the square root of the dislocation density, satisfying the Taylor relationship. In other words, the elementary process of plastic deformation involves dislocations cutting through Hayashi dislocations and plastic deformation progressing through dislocations in UFG material with a grain size of 500 nm. In addition, as shown in Fig. 9.5, the 50 nm nickel nanocrystals exhibit the same trend as that of aluminum with grain sizes of 500 nm to 20 μm, suggesting that plastic deformation progresses through dislocations up to a grain size of 50 nm.

It is difficult to obtain nanocrystalline materials with a crystal grain size of 50 nm or lower from pure metals by using an electrolytic deposition method; thus, alloying is required. Here, a nanocrystalline Ni–W alloy is developed in an electrolytic bath containing nickel sulfate hexahydrate and sodium tungstate (Nakayama et al. 2016;

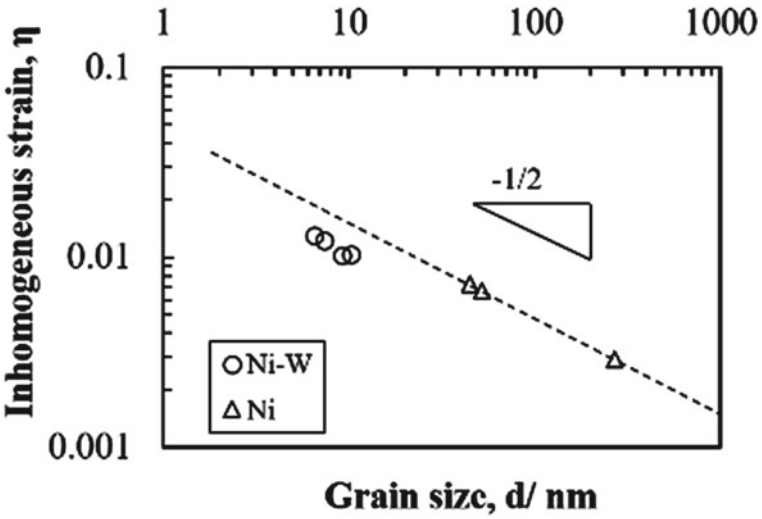

Fig. 9.8 The inhomogeneous strains as a function of grain size for NC-Ni and Ni-W alloys

Schuh et al. 2002; Yamasaki 2000, 1999). It is possible to change the W content by changing the ratios of nickel sulfate hexahydrate and sodium tungstate, and in this way, four alloys can be obtained: Ni-4.0at.%W, Ni-5.3at.%W, Ni-8.3at.%W, and Ni-9.8at.%W, with crystal grain sizes of 10.3, 9.2, 7.4, and 6.5 nm, respectively, and it is evident that the increase in W content decreases the crystal grain size. Figure 9.8 shows the changes in inhomogeneous strain, ε, during tensile deformation of the Ni-8.3at.%W alloy, which is a material with a grain size of a single nanometer. Assuming that this inhomogeneous strain occurs due to dislocations, the dislocation density can be obtained by substituting the inhomogeneous strain into Eq. (9.1). However, here the inhomogeneous strain is shown, which does not increase up to 2% macrostrain, indicating that the system is in region I, where only elastic deformation occurs. After that, the system enters region II, where the inhomogeneous strain increases linearly up to 5% macrostrain. At 5% macrostrain and above, changes in the inhomogeneous strain decelerate, indicating that the system is in region III. Based on the above observations, plastic deformation clearly occurs due to plastrons which generate inhomogeneous strain.

Denoting the inhomogeneous strain between regions II and III by ε_{II}, Fig. 9.8 shows the changes in ε_{II} due to the changes in the crystal grain sizes in the nanocrystalline Ni–W alloy. The figure also shows the εII values for nanocrystalline nickel obtained by the electrolytic deposition method and the UFG nickel obtained by the ARB method. As is clear from Fig. 9.5, ρII is proportional to the inverse of the grain size for pure nickel, so ε_{II} is proportional to the inverse of the square root of the grain size, as in Eq. (9.1). In Fig. 9.8, the ε_{II} value of the nanocrystalline Ni–W alloy is around 30–40% smaller than the dotted line with a slope value of − 1/2 for pure nickel. Assuming that the plastic deformation progresses through dislocations,

it can be surmised that the dislocation density from Eq. (9.1) is as low as 1/3–1/2 of the extrapolated values and that the deformation in the nanocrystalline Ni–W alloys with grain sizes of 6.5–10.3 nm does not progress through dislocations. If the plastic deformation in the nanocrystalline Ni–W alloys progresses through dislocations, the inhomogeneous strain is predicted by the extrapolation and the value of the dislocation density ρ_{II} necessary for plastic deformation to occur is almost 10^{17} m^{-2}. In this case, the strain energy in the grains becomes extremely high, making it likely that the plastic deformation progresses through a plaston with a lower inhomogeneous strain than dislocation.

What is the plaston in the nanocrystalline Ni–W alloy? As suggested by some molecular dynamics calculations, it is thought that partial dislocations have been activated (Yamasaki 1999; Yamakov et al. 2001). As is apparent from Eq. (9.1), the inhomogeneous strain is proportional to the square of the Burgers vector. For this reason, the activity of partial dislocations having a small Burgers vector suppresses the increase in the strain energy inside the grains, so the plaston in the single nanometer grain material is equivalent to a partial dislocation. In contrast, even though there are complete dislocation activities in materials ranging from CG aluminum to NC nickel, the total strain energy is relatively low, so the plastons are perfect dislocations. It has been reported that the addition of W to pure Ni reduces the stacking fault energy, and that the value for the Ni-10at.% W alloy is half that of pure Ni. In the Ni-10at.%W alloy (Suto and Kuniaki 1971), when the edge dislocations, which are complete dislocations, decompose into partial dislocations, the ditch of the lamination defect becomes ~ 5–6 nm. This is close to the crystal grain size, which makes it easier for partial dislocations to occur in the Ni–W alloy.

Figure 9.9 shows the changes in the 0.2% proof stress upon a change in the initial strain rate during tensile deformation in nanocrystalline nickel with a grain size of 50 nm and the Ni-5.3at.%W alloy with a grain size of 9.2 nm. The values of the strain rate sensitivity index, m, are found to be 0.036 and 0.026, respectively. It is known that an m value of greater than 0.3 occurs during boundary sliding and that of 1 occurs during Coble creep (Coble 1963). The m values are much lower than either of the above two values, which indicates that for materials with a single nanometer grain size at room temperature, the deformation does not progress through boundary sliding or creep, which is in good agreement with the in situ XRD results.

In coarse-grain materials, the Frank–Read source in the grains is the main dislocation source, but as the crystal grain becomes finer, the stress for generating dislocation from the Frank–Read source gradually increases. The dislocations bow out from the source, and since the stress required for increasing dislocations is inversely proportional to the source length, sources with longer source lengths can increase dislocations with lower stress. However, dislocations cannot bow out into the grains unless the source length is about a third of the grain size or smaller, and since the stress is inversely proportional to the grain size, the stress increases at an accelerated rate as the crystal grain size becomes finer. In UFG materials, the dislocation source shits at to the grain boundaries because the dislocation generation stress decreases (Kato et al. 2008; Kato 2009). The in situ XRD measurements mentioned above show that intra-grain dislocations are annihilated with the grain boundary because

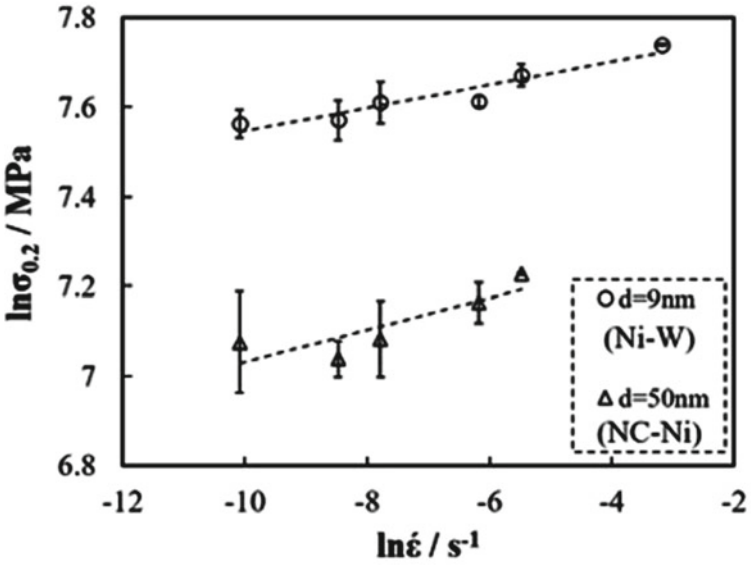

Fig. 9.9 Relationship between 0.2% proof stress and initial strain rate for NC-Ni and Ni-W alloys

of the sink occurring during unloading associated with fracture. From this, we can easily surmise that the grain boundary becomes a dislocation source. However, the grain boundary structure changes to a stable structure along with the dislocations emission, so it can be predicted that the grain boundary cannot emit dislocations without limit. In nanocrystalline nickel with a grain size of 50 nm formed by an electrolytic deposition method and the Ni–W alloy with a single nanometer grain size, the crystal grain size hardly changes due to the materials being kept at room temperature for a long time or being exposed to low-temperature annealing at around 373 K, but plastic elongation dramatically decreases. This suggests that, while the grain boundary of the nanocrystalline material developed by the electrolytic deposition method is at non-equilibrium and has a high potential for emitting dislocations, the potential decreases as the grain boundary structure becomes stable due to low-temperature annealing. How, then, can the dislocation release potential of the grain boundary be improved?

It is surmised that there is a limit to the extent of emit from the grain boundary in nanocrystalline materials, which is one of the causes for the low ductility of nanocrystalline materials. Attempts have been made to improve ductility by improving the dislocation emitted from the grain boundary. In other words, it is thought that the dislocation release potential can be improved by creating two phases of nanocrystalline and amorphous states, thereby placing a wide amorphous phase on the grain boundary of nanocrystals (Nakayama et al. 2016). It was previously mentioned that the W content in the Ni–W alloy can be changed by changing the ratios of nickel

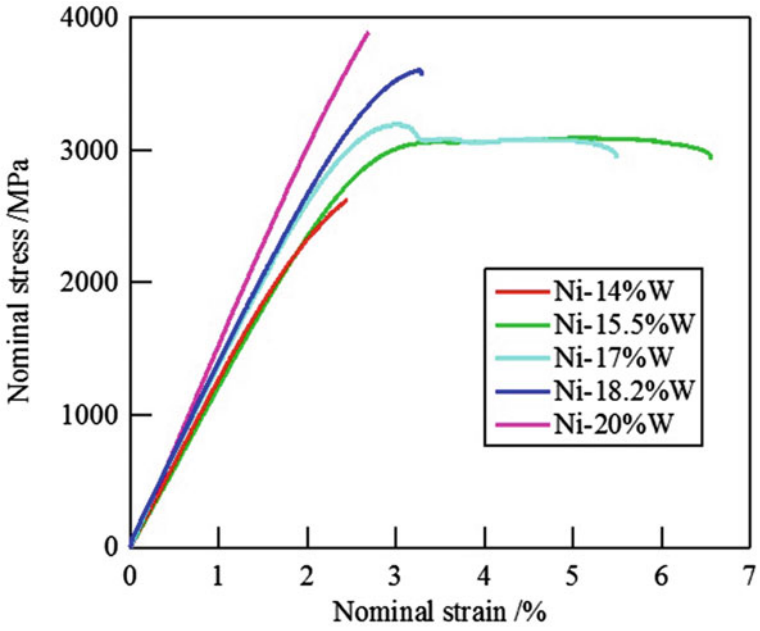

Fig. 9.10 Nominal stress–strain curves for Ni-W alloys with W contents between 14 and 20 at. %. Reprinted with permission from (Nakayama et al. 2016), Copyright 2016, American Scientific Publishers

sulfate hexahydrate and sodium tungstate in the electrolytic bath. The nanocrystalline single phase is maintained up to a W concentration of 14at%W, and the amorphous single phase takes over once it exceeds 20at%W. At ~14–20at%W, two phases, nanocrystalline and amorphous, can be obtained, and their proportion can be continuously changed by altering the W concentration. In addition, the grain size of the nanocrystals is an approximately constant value, at ~5 nm. Figure 9.10 shows the changes in the stress–strain curves due to changes in the W concentration in Ni–W alloys with nanocrystalline and amorphous phases. There is little ductility in the nanocrystalline single-phase Ni-14at%W and amorphous single-phase Ni-20at% alloys, but ductility is obtained in materials with nanocrystalline and amorphous phases. The Ni-17at%W alloy has a tensile strength of 2.5 GPa and a stretch of 4%, showing high strength and ductility. This is likely because the many amorphous regions in the grain boundaries of the nanocrystals increase the dislocation emit from the grain boundary, maintaining the plastic deformation.

Figure 9.11 shows the results of in situ XRD measurements on the Ni-17at%W alloy, for which because it is a two-phase alloy with nanocrystalline and amorphous phases, only a very wide (111) diffraction peak can be observed. This shows the change in the full width at half maximum (FWHM) of the (111) diffraction peak. It is evident that the FWHM suddenly decreases after the yield point, which implies that plastic deformation reduces the amorphous phase and increases the crystalline phase.

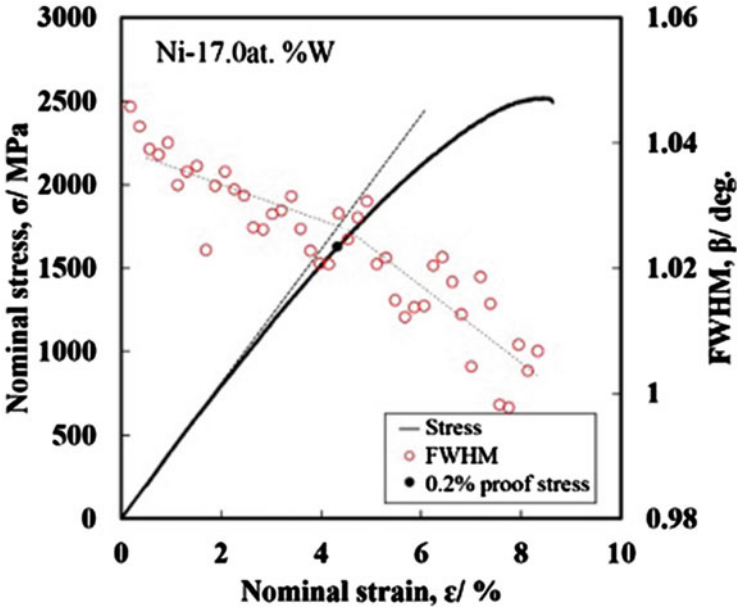

Fig. 9.11 Change in the FWHM of the Ni (111) peak as a function of nominal strain for Ni-12.7at.%W alloy during in situ XRD. Reprinted with permission from (Nakayama et al. 2016), Copyright 2016, American Scientific Publishers

An electron microscopy observation of the structure under tensile deformation with 5% plastic strain reveals that the nanocrystalline grain size increases, compared to that before the application of tension, by 1.1 nm. This suggests that the amorphous phases at the boundary of the nanocrystalline and amorphous phases become crystallized due to plastic deformation. In other words, as partial dislocations arise from the nanocrystalline and amorphous boundary during plastic deformation, the amorphous phase at the boundary becomes stable and changes its structure to FCC (Swygenhoven et al. 2002), upon which it is thought that the nanocrystals grow as a result.

References

Adachi H, Karamatsu Y, Nakayama S, Miyazawa T, Sato M, Yamasaki T (2016) Mater Trans 57:1447–1453
Adachi H, Miyajima Y, Sato M, Tsuji N (2015) Mater Trans 56:671–675
Adachi H, Mizowaki H, Hirata M, Okai D, Nakanishi H (2021) Mater Trans 62(1), in print
Adachi H, Mizowaki H, Hirata M, Okai D, Nakanishi H (2020) J JILM 70:274–280
Bailey JE, Hirsch PB (1960) Philos Mag 5:485–497
Budrovic Z, Swygenhoven HV, Derlet PM, Petegem SV, Schmitt B (2004) Science 304:273–276
Chen M, Ma E, Hemker KJ, Sheng H, Wang Y, Cheng X (2003) Science 300:1275–1277
Coble RL (1963) J Appl Phys 34:1679–1682

Dao M, Lu L, Asaro RJ, De Hosson JTM, Ma E (2007) Acta Mater 55:4041–4065
Ferrasse S (1997) Metall Mat Trans A 28:1047–1057
Fleischer RL (1963) Acta Metall 11:203–209
Gerold V, Harberkorn H (1966) Phys Stat Sol 16:675–685
Hall EQ (1951) Proc Phys Soc London B 64:747–751
Horita Z, Langdon TG (2005) Mater Sci Eng A 410–411:422–425
Huang X, Hansen N, Tsuji N (2006) Science 312:249–251
Huang X, Tsuji N, Hansen N, Minamino Y (2003) Mater Sci Eng A 340:265–271
Kamikawa N, Tsuji N, Saito Y (2003) Tetsu-to-Hagane 89:273–280
Kamikawa N, Huang X, Tsuji N, Hansen N (2009) Acta Mater 57:4198–4208
Kato M (2009) Mater Sci Eng A 516:276–282
Kato M, Fujii T, Onaka S (2008) Mater Trans 49:1278–1283
Liao XZ, Kilmametov AR, Valev RZ, Gao H, Li X, Mukherjee AK, Bingert JF, Zhu YT (2006) Appl Phys Lett 88:021909
Lu L, Schwaiger R, Shan ZW, Dan M, Lu K, Suresh S (2005) Acta Mater 53:2169–2179
Miyajima Y, Okubo S, Miyazawa T, Adachi H, Fujii T (2016) Philos Mag Lett 96:294–304
Mompiou F, Cailard D, Legros M, Mughrabi H (2012) Acta Mater. Col 60:3402–3414
Nakayama S, Adachi H, Nabeshima T, Miyazawa T, Yamasaki T (2016) Sci Adv Mater 8:2082–2088
Petch NJ (1953) J Iron Steel Inst 174:25–28
Schuh CA, Nieh TG, Yamasaki T (2002) Scripta Mater 46:735–740
Shen YF, Lu L, Lu QH, Jin ZH, Lu K (2005) Scripta Mater 52:989–994
Suto H, Kuniaki K (1971) J Jpn Inst Met 35:231–237
Swygenhoven HV, Spaczer M, Caro A (1999) Acta Mater 47:3117–3126
Swygenhoven HV, Derlet PM, Hasnaoui A (2002) Phys Rev B 66:024101
Tsuji N, Ito Y, Saito Y, Minamino Y (2002) Scripta Mater 47:893–899
Valiev RZ, Islamgaliev RK, Alexandrov IV (2000) Rrog Mater Sci 45:103–189
Williamson GK, Hall WH (1953) Acta Metall 1:23–31
Williamson GK, Smallman RE (1954) Acta Crystallogr 7:574–581
Williamson GK, Smallman RE (1956) Philos Mag 8:34–45
Yamakov V, Wolf D, Salazar M, Phillpot SR, Gleiter H (2001) Acta Mater 49:2713–2722
Yamasaki T (1999) J Jpn Inst Met Mater 69:404–412
Yamasaki T (2000) Mater Phys Mech 1:127–132

Open Access This chapter is licensed under the terms of the Creative Commons Attribution 4.0 International License (http://creativecommons.org/licenses/by/4.0/), which permits use, sharing, adaptation, distribution and reproduction in any medium or format, as long as you give appropriate credit to the original author(s) and the source, provide a link to the Creative Commons license and indicate if changes were made.

The images or other third party material in this chapter are included in the chapter's Creative Commons license, unless indicated otherwise in a credit line to the material. If material is not included in the chapter's Creative Commons license and your intended use is not permitted by statutory regulation or exceeds the permitted use, you will need to obtain permission directly from the copyright holder.